

1 The spectral underpinnings of pathogen spread on animal networks

2 **Authors:** Nicholas M. Fountain-Jones^{1*}, Mathew Silk^{2,3}, Raima Appaw¹, Rodrigo Hamede¹,
3 Julie Rushmore⁴, Kimberly VanderWaal⁵, Meggan Craft⁶, Scott Carver¹ & Michael
4 Charleston¹

5 Affiliations:

⁶ ¹School of Natural Sciences, University of Tasmania, Hobart Australia 7001.

7 ²CEFE, University of Montpellier, CNRS, EPHE, IRD, University of Paul Valéry
8 Montpellier 3, Montpellier, France

⁹ ³Centre for Ecology and Conservation, University of Exeter, Penryn Campus, Penryn, UK

⁴Odum School of Ecology, University of Georgia, Athens, GA USA.

⁵ Department of Veterinary Population Medicine, University of Minnesota, St Paul, MN, USA

15

16 *Nick.FountainJones@utas.edu.au

17

18

19
20 Predicting what factors promote or protect populations from infectious disease is a
21 fundamental epidemiological challenge. Social networks, where nodes represent hosts and
22 edges represent direct or indirect contacts between them, are key to quantifying these aspects
23 of infectious disease dynamics. However, understanding the complex relationships between
24 network structure and epidemic parameters in predicting spread has been out of reach. Here
25 we draw on advances in spectral graph theory and interpretable machine learning, to build
26 predictive models of pathogen spread on a large collection of empirical networks from across
27 the animal kingdom. Using a small set of network spectral properties, we were able to predict
28 pathogen spread with remarkable accuracy for a wide range of transmissibility and recovery
29 rates. We validate our findings using well studied host-pathogen systems and provide a

30 flexible framework for animal health practitioners to assess the vulnerability of a particular
31 network to pathogen spread.

32

33 **Introduction**

34
35 Capturing patterns of direct or indirect contacts between hosts is crucial to model pathogen
36 spread in populations (Newman 2002; Craft 2015; Sah *et al.* 2018, 2021). Increasingly,
37 contact network approaches, where hosts are nodes and edges reflect interactions between
38 hosts, play a central role in epidemiology and disease ecology (e.g., Meyers *et al.* 2005;
39 Bansal *et al.* 2007; Eames *et al.* 2015; White *et al.* 2017). Incorporating networks allows
40 models to capture the heterogeneity of contacts between individuals that can provide more
41 nuanced and reliable estimates of pathogen spread, including in wildlife populations (e.g.,
42 Meyers *et al.* 2006; Bansal *et al.* 2010; Craft *et al.* 2011). Formulating general rules for how
43 easy-to-calculate network structure properties may promote or restrict pathogen spread can
44 reveal important insights into how host behaviour can mediate epidemic outcomes (Sah *et al.*
45 2017), and provide practitioners with a proxy for how vulnerable a population is to disease
46 without extensive simulations (Silk *et al.* 2017; Sah *et al.* 2018). Further, network structural
47 properties can be incorporated into traditional susceptible–infected–recovered (SIR) models
48 to account for contact heterogeneity when predicting pathogen dynamics across populations
49 (e.g., Meyers *et al.* 2005; Bansal *et al.* 2007).

50

51 However, it remains unclear whether one structural characteristic or a combination of
52 characteristics can reliably predict pathogen dynamics across systems (Ames *et al.* 2011; Sah
53 *et al.* 2018). For example, species that are more social tend to have more clustered or
54 “modular” networks, and this modularity has been found to increase (Lentz *et al.* 2012),
55 reduce (Salathé & Jones 2010) or have little effect (Sah *et al.* 2018) on outbreak size across

56 different biological systems. The average number of contacts between hosts can be identical
57 across networks and yet still result in substantially different outbreak patterns (Ames *et al.*
58 2011). Even the apparent size of the network, often constrained by limitations of sampling,
59 can impact estimates of pathogen spread, particularly in wildlife populations (McCabe &
60 Nunn 2018). As network characteristics, such as network size and modularity, are often
61 correlated (Newman 2006; Silk *et al.* 2017) and can have complex impacts on spread (Sah *et*
62 *al.* 2017; McCabe & Nunn 2018; Porter 2020), determining network characteristics that
63 promote large outbreaks, for example, remains a fundamental question in infectious disease
64 biology (Sah *et al.* 2018).

65

66 Searching for general relationships between network structure and pathogen spread in animal
67 populations is further challenged, as the relationship is also affected by pathogen traits, such
68 as infectiousness and recovery rate. For example, modularity appears to make no difference
69 to disease outcomes for highly infectious pathogens (Sah *et al.* 2017). Diseases with long
70 recovery rates can increase outbreak size across networks as well (Shu *et al.* 2016). Given
71 that we rarely have reliable estimates of pathogen traits in wild populations (e.g., for different
72 probabilities of infection per contact, or recovery rates) anyway, any predictive model of the
73 relationship between spread and network structure would ideally be generalizable across
74 pathogens.

75

76 Advances in spectral graph theory offer an additional set of measures based on the **spectrum**
77 of a network rather than average node or edge level attributes. A graph spectrum is the set of
78 **eigenvalues** (often denoted with a Greek lambda λ) of a matrix representation of a network
79 (see Text Box 1 for further definitions for terminology in bold). Theoretical studies have
80 shown relationships between particular eigenvalues and connectivity across networks are

81 independent of pathogen propagation models (Prakash *et al.* 2010). For example, networks
82 with a high **Fiedler value** (the second smallest eigenvalue of the network's **Laplacian**
83 **matrix**) are “more connected” than those with low values. It has been found that, in
84 ecological networks for example, if the Fiedler value is sufficiently large, removing edges
85 will have little effect on overall network connectivity (Kumar *et al.* 2019), but whether this
86 lack of effect is mirrored by pathogen dynamics is not yet clear. Another quantity of interest
87 is **spectral radius** – the largest absolute value of the eigenvalues of its **adjacency matrix**.
88 The link between the spectral radius and epidemiological dynamics is better understood, with
89 theoretical work showing that this value closely mirrors both epidemic behaviour and
90 network connectivity (Prakash *et al.* 2010) and has been used to understand vulnerability of
91 cattle networks to disease (Darbon *et al.* 2018). For example, networks with the same number
92 of edges and nodes but higher spectral radius (λ_1) are more vulnerable to outbreaks than
93 networks with low spectral radius ($\lambda_1 \rightarrow 1$). We hypothesize that spectral measures such as
94 these have great potential to improve our ability to predict dynamics of pathogen spread on
95 networks, where previous methods such as modularity have proved inadequate (Sah *et al.*
96 2017).

97
98 We assess the predictive capability of spectral values compared to other structural attributes
99 such as **modularity** (Newmans' Q ; Newman 2006)) using advances in machine learning to
100 construct non-linear models of simulated pathogen spread across a large collection of
101 empirical animal networks including those from the Animal Social Network Repository
102 (ASNR) (Sah *et al.* 2019). The ASNR is a large repository of empirical contact networks that
103 provides novel opportunities to test the utility of spectral values in predicting spread across a
104 wide variety of, mostly animal, taxa across a spectrum of social systems -- from eusocial ants
105 (Arthropoda: Formicidae) to more solitary species such as the desert tortoise (*Gopherus*

106 *agassizii*). Farmed domestic animals were not included in our analyses. We combined
107 networks from this resource with other published networks, including badgers (*Meles meles*)
108 (Weber *et al.* 2013), giraffes (*Giraffa camelopardalis*) (VanderWaal *et al.* 2014) and
109 chimpanzees (*Pan troglodytes*) (Rushmore *et al.* 2013) to generate a dataset of over 600
110 unweighted networks from 51 species. We then simulated pathogen spread using a variety of
111 SIR parameters and harnessed recent advances in multivariate interpretable machine learning
112 models (*MrIML*; (Fountain-Jones *et al.* 2021)) to construct predictive models across SIR
113 parameter space. As many species were represented by multiple networks, often over
114 different populations and or timepoints and constructed in different ways (e.g., some edges
115 reflected spatial proximity rather than direct contact), we included species and network
116 construction variables in our models to account for these correlations in addition to exploring
117 the diversity of network structures across the animal kingdom. Our interpretable machine
118 learning models identify putative threshold values for the vulnerability of a network to
119 pathogen spread that can be used by practitioners to understand outbreak risk across systems.

120
121 We test how well our network structure estimates of pathogen spread, trained on SIR
122 simulation results, generalize to more complex pathogen dynamics in the wild. We utilize
123 two well studied wildlife-pathogen systems to assess how our predictions compare to
124 empirical estimates of spread; *Mycobacterium bovis* (the bacterium that causes bovine
125 tuberculosis (bTB)) in badger populations and devil facial tumour disease (DFTD) in
126 Tasmanian devil (*Sarcophilus harrisii*) populations (Hamede *et al.* 2009). We demonstrate
127 that using spectral measures of network structure alone can provide a useful proxy for disease
128 vulnerability with estimates of prevalence comparable to those empirically derived. Further,
129 we provide a user-friendly app that utilizes our models to provide practitioners with
130 predictions, for example, of the prevalence of a pathogen across a variety of spread scenarios

131 using a user-supplied network without the need for lengthy simulation. The url for this

132 “Shiny” app is <https://spreadpredictr.shinyapps.io/spreadpredictr/>.

133

134 **Text Box 1:** Terminology used in this paper.

135 A *graph* (or “*network*”) is a collection of *nodes* and a collection of *edges* connecting the
136 nodes in pairs, e.g., nodes x, y joined by edge (x,y) . We define the *size* of the network –
137 usually n , as the number of nodes (this usage differs from other strict mathematical
138 definitions, but we feel this is more intuitive). Two nodes are said to be *adjacent* if they are
139 connected by an edge, and the number of vertices adjacent to a given vertex x is called its
140 *degree*, $\deg(x)$. Edges may be directed, in which case edge (x,y) is different from edge (y,x) ,
141 but in our analyses we treat them as *undirected*, so $(x,y)=(y,x)$. Graphs can be represented
142 naturally by matrices whose rows and columns are indexed by the nodes $(1,2,\dots,n)$: the
143 obvious one is the *adjacency matrix* A , whose (i,j) -th entry A_{ij} is 1 if nodes i and j are
144 adjacent, and 0 otherwise. A is symmetric and $n \times n$, as are all the matrices in this work.

145 Another useful matrix is the *degree matrix* D , in which D_{ij} is the degree of node i if $i=j$, and 0
146 otherwise. The *Laplacian* matrix L is the most complex one we use herein, but is easily
147 calculated using $L_{ij} = D_{ij} - A_{ij}$.

148 The *eigenvalues* of a matrix are solutions to the matrix equation $M\mathbf{v} = \lambda\mathbf{v}$, where M is a
149 matrix and \mathbf{v} a vector of the appropriate size. Solving for \mathbf{v} yields λ . These eigenvalues,
150 ordered by their size, form the *spectrum* of a graph, as derived using any of the matrices just
151 described. The *Fiedler value* of a graph is the second-smallest eigenvalue of L , and the
152 *spectral radius* is the largest eigenvalue of A .

153 Measures of *Modularity* such as the Newman Q coefficient capture the strength of division
154 within a network by quantifying the density of edges within and between subgroups. When
155 there is no division within the network as the density of edges is the same between and within
156 subgroups $Q = 0$, whereas higher values of Q indicate stronger divisions (Newman 2006). As
157 Q scales with network size (small networks being generally less modular), relative

158 modularity (Q_{rel}) allows for comparison across network sizes by normalizing Q using the

159 maximum possible modularity for the network (Q_{max}) (Sah *et al.* 2017).

160

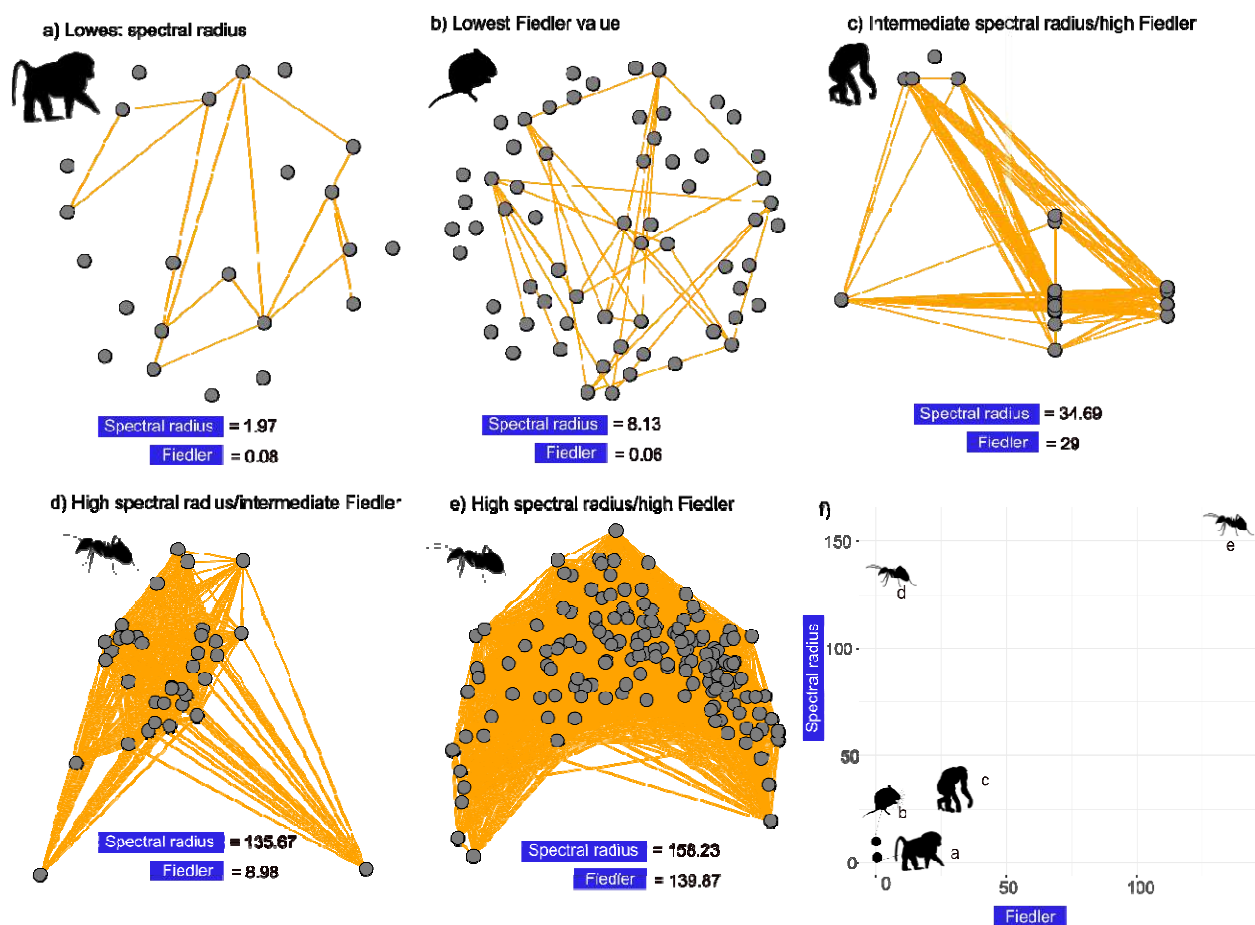
161 **Results**

162

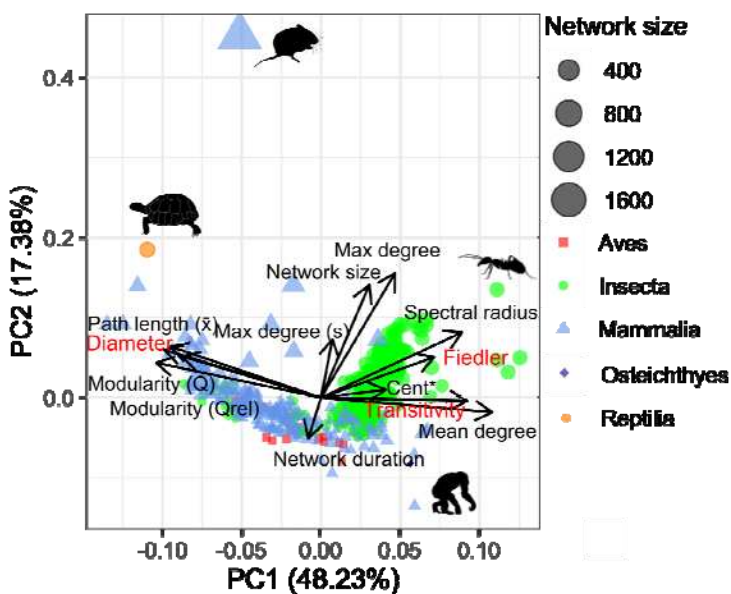
163 *Diversity of network structures*

164 We identified substantial variation in network structure across animal taxa. The static
165 unweighted animal social networks in our database ranged from nearly completely
166 unconnected (Spectral radius $\lambda_1 \sim 1$, Fiedler value ~ 0 , not included in our predictive models)
167 to highly connected (Spectral radius $\lambda_1 \sim 160$, Fiedler value ~ 140 , Fig. 1). Similarly, the
168 networks ranged from homogeneous (i.e., not modular, $Q_{\text{rel}} = 0$, see the Text box for a
169 definition) to highly modular and subdivided ($Q_{\text{rel}} > 0.8$). Our principal component analysis
170 (PCA) identified key axes of structural variation across empirical networks (Fig. 2). The first
171 principal component (PC1) distinguished networks that had a large diameter and mean path
172 length and were highly modular (negative values), from networks with a high mean degree
173 and transitivity (positive values, Fig. 2, see Table S2). The second principal component (PC2)
174 separated networks based on network size (number of nodes), maximum degree and the
175 network duration (i.e., the time period over which the network data was collected, Fig. 2).
176 The eusocial ant networks (*Camponotus fellah*, Insecta: Hymenoptera) and mammal
177 networks tended to cluster separately (Fig. 1), with the other taxonomic classes dispersed
178 between these groups (Fig. 1) or species (see Fig. S1 for clustering by species). The
179 networks' spectral properties (the Fiedler value and spectral radius) explained a unique
180 portion of structural variance that did not covary with other variables (see Table S1 for vector
181 loadings and Fig S2 for all pair-wise correlations). We found variables such as mean degree
182 and transitivity the most correlated with the other variables and were excluded from further
183 analysis (Tables S2, Fig S2).

184



185
186 **Fig.1:** Examples of networks analysed in this study with a) the lowest spectral radius
187 (baboons *Papio cynocephalus* contact network), b) the lowest Fiedler value (voles *Microtus*
188 *agrestis* trap sharing network), c) intermediate spectral radius values but high Fiedler value
189 (Chimpanzee *Pan troglodytes* contact network), d) high spectral radius/intermediate Fiedler
190 value (*Camponotus fellah* colony contact network) and e) high values of both measures
191 (another *C. fellah* colony contact network). The mean values across all networks were 34.80
192 and 7.31 for the spectral radius and Fiedler value respectively. f) summary of values across
193 networks (a-e). Silhouettes were sourced from phylopic (<http://phylopic.org/>). Note that
194 disconnected nodes were not included in the analysis.
195



196

197 **Fig. 2:** Principal components analysis (PCA) biplot showing that network structure largely
198 clusters by taxonomic class. Points are coloured by taxa. Points closer together in Euclidean
199 space have networks more similar in structure. Points are scaled by network size. The length
200 and direction of vectors (black arrows) shows how each variable relates to each principal
201 component with larger vectors having higher loadings on that axis. The PCA was constructed
202 just using continuous network characteristics. Percentages next to PC scores indicate how
203 much variability in the data is accounted for by each axis. Cent*: Centralization. See Table
204 S1 for axis loadings and Fig. S1 for the species-level clustering. See Tables S2 & S3 for
205 variable definitions. Silhouettes for some of the outlying networks were sourced from
206 phylopic (<http://phylopic.org/>). s = scaled. Cent = Centralization.

207

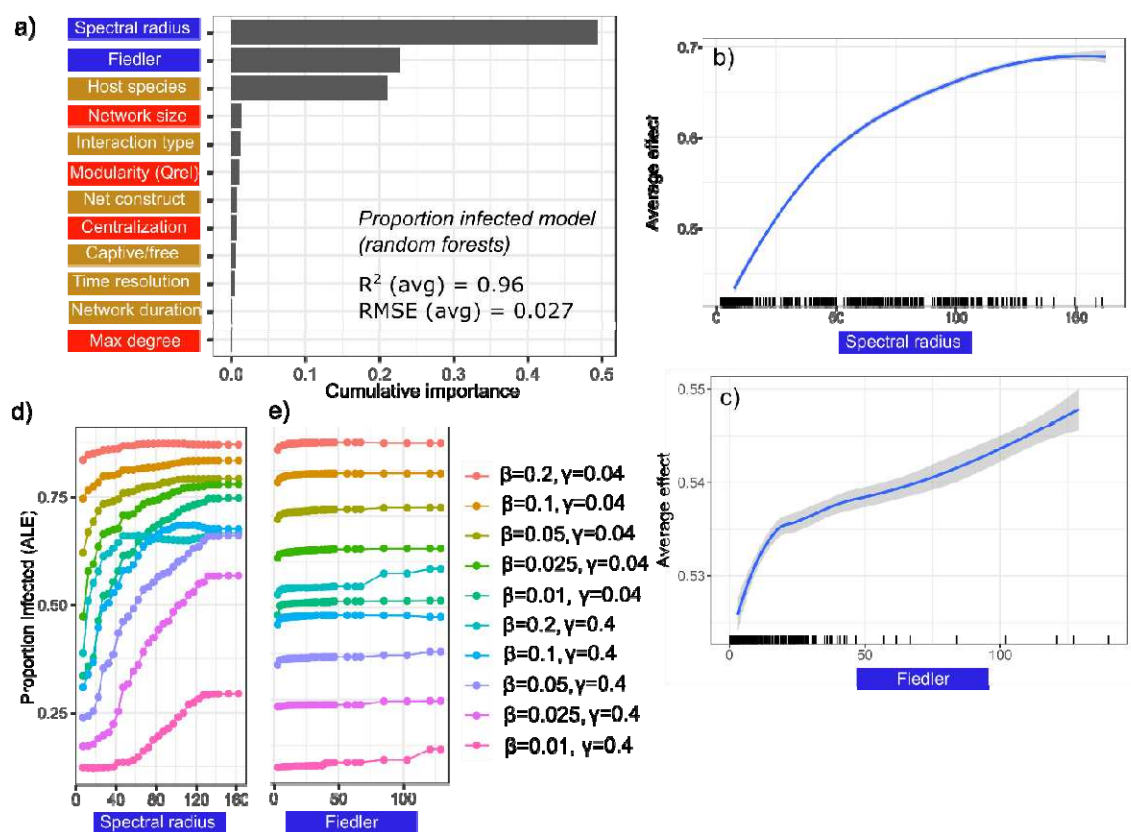
208 *Spectral properties predict pathogen spread across epidemic scenarios*

209

210 We found that network characteristics alone could predict pathogen transmission dynamics
211 remarkably well (Figs. 3 & Fig S3). We constructed models in *MrIML* to predict the
212 maximum proportion of nodes infected in the network over 100 time steps (hereafter
213 ‘proportion infected’). With these models we could predict the proportion infected in a
214 network using both spectral measures and species identity alone (Fig. 3a). Network size,
215 relative modularity and centralization, for example, were less important in predicting
216 proportion infected across all SIR model parameter combinations tested (Fig. 2a). Nonlinear
217 relationships were likely important for prediction of proportion infected, as random forests

218 (RF) had the highest predictive performance overall (Table S4) and substantially
219 outperformed linear regression in the *MrIML* framework (root mean square error (RMSE)
220 0.13 vs 0.03). Variable importance and predictor conditional effects were consistent between
221 the machine learning algorithms, so we subsequently analysed the best performing RF model.
222 Across all SIR parameter combinations, we found a nonlinear relationship between
223 proportion infected and spectral radius, with the average prediction of proportion infected
224 increasing by ~30% across the range of spectral radius values (holding all other variables
225 constant in the model, Fig. 3b). In contrast we found a more modest effect of the Fiedler
226 value, with the proportion of infected only increasing on average ~3% across the observed
227 range of values for all SIR parameters (Fig 3c). We did find a sharp increase in the proportion
228 infected in networks when the Fiedler value was less than about 15 (Fig. 3c). However, there
229 was variation in the relationship between the proportion infected and these spectral values
230 across transmission (β) and recovery probabilities (γ , Figs. 3d-e). For example, when the
231 probability of transmission was relatively high ($\beta = 0.2$) and recovery low ($\gamma = 0.04$) the
232 proportion infected across networks was ~80% and spectral radius had a relatively minor
233 effect (Fig. 3d). A network's spectral radius had a stronger effect when the probability of
234 recovery was higher ($\gamma = 0.4$) across all values of β . The increase in proportion infected when
235 the Fiedler value was low (< 15) was not apparent when spread was slower and chances of
236 recovery higher (e.g., $\beta = 0.025$ or 0.01, $\gamma = 0.4$; Fig 3e). The spectral radius and Fiedler
237 value patterns overall were similar, with larger values reducing the time-to-peak prevalence
238 (hereafter 'time to peak', Fig. S3). However, modularity played a greater role in our time to
239 peak models, with the time to peak being longer for more modular networks above a Q_{rel}
240 threshold of ~ 0.75 (Fig. S4).

241



242 **Fig. 3:** Plots showing the predictive performance, variable importance and the functional
243 form of relationships for our best-performing *MrIML* proportion infected model. See Table
244 S4 for model performance estimates across algorithms. The colour of the labels indicates
245 what type of predictor it is (blue = spectral, red = non-spectral network structural variables,
246 gold = network metadata, see Tables S2 & S3). a) Spectral radius and the Fiedler value
247 (followed by species) are the most important predictors of proportion of individuals infected
248 across all simulations (importance threshold >0.1) and overall model performance was high
249 ($R^2 = 0.96$ and root mean square error (RMSE) = 0.027). b-c) Average predictive
250 surface showing the relationship between spectral properties and proportion infected across
251 all epidemic values (95% confidence intervals in grey). Rug plot on the x axis of the panels
252 on the right shows the distribution of each characteristic across empirical networks. d-e) The
253 accumulated local effects (ALE) plot revealed that the strongly non-linear relationships
254 between both spectral properties and proportion infected were mediated by transmission and
255 recovery probabilities. We chose these SIR parameter values (β = transmission probability, γ
256 = recovery probability) to ensure major outbreaks occurred on the empirical networks. Net
257 construct = Network construction method.

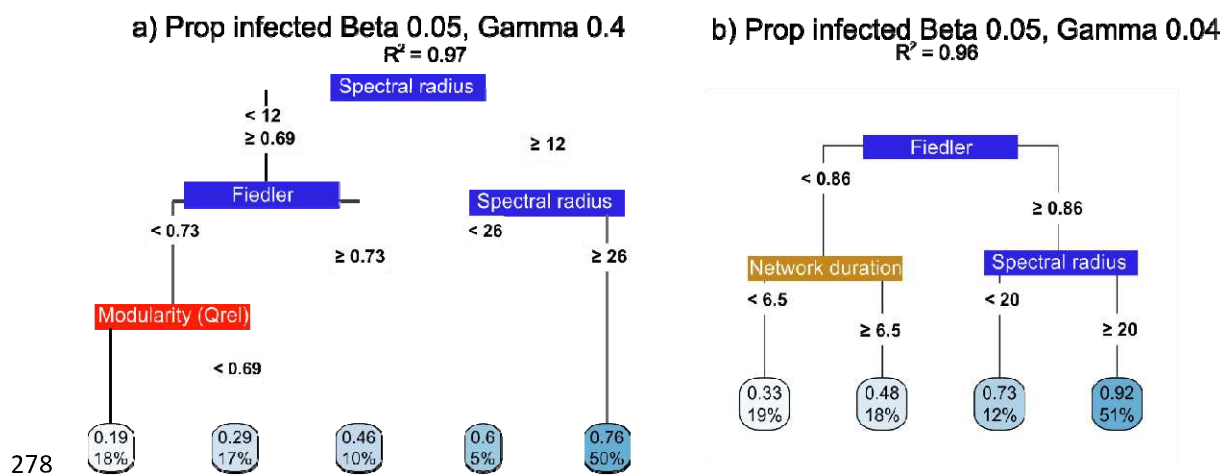
259

260 *Simplifying our models with global surrogates*

261

262 When we further interrogated our moderate ($\beta = 0.05$) transmission models, we found that the
263 spectral radius and Fiedler value overall also played a dominant role in our predictions of
264 spread. To quantify the putative mechanisms that underlie our model predictions – ‘to
265 decloak the black box’ – and gain insight into possible interactions between predictors, we
266 constructed surrogate decision trees as a proxy for our more complex RF model. We trained
267 our surrogate decision tree on the predictions of the RF model rather than the network
268 observations directly. In each case, the surrogate decision tree approximated the predictions
269 of our models (thousands of decision trees) remarkably well (Global $R^2 > 0.95$, see (Molnar
270 2018) for details). The spectral radius and, to a lesser extent, the Fiedler value and modularity
271 values dominated surrogate trees for all SIR parameter sets (Fig. 5, Figs. S5 & S6). For
272 example, for networks with a Fiedler value ≥ 0.86 and a spectral radius ≥ 20 (as was the case
273 for 51% of our networks, Fig. 4b) the estimated maximum proportion of the network infected
274 was 0.92 (Fig. 4b). The duration over which the data was collected also was included in the
275 surrogate model, with networks collected over > 6.5 days having higher estimates of
276 proportion infected (Fig. 4b).

277



279 **Fig. 4** Global surrogate decision trees for our moderate transmission ($\beta = 0.05$) proportion
280 infected with a) high and b) low recovery probability ($\gamma = 0.4$ and 0.04 respectively).
281 Threshold values of each variable are included in each tree. The boxes at the tips of the trees
282 indicate the estimates of average peak time or proportion of the network infected across
283 simulations (top value) and percentage of networks in our dataset to be assigned to this tip.
284 For example, 50% of our empirical networks had spectral radius values ≥ 26 and for these
285 networks we found on average, a maximum of 0.76 of the network infected after 100 time
286 steps. Tip boxes are coloured light to dark blue based on network vulnerability to pathogen
287 spread (e.g., longer time to peak = light blue). Global fit = R^2 for how well the surrogate
288 model replicates the predictions of the trained model. See Figs. S5 for the complete list of
289 global surrogate models and Fig. S6 for ‘time to peak’ surrogates. Colour of the label
290 indicates what type of predictor it is (blue = spectral, red = non-spectral structural variables,
291 gold = network metadata, see Tables S2 & S3).

292

293 *Do our structural estimates generalize to more complex spread scenarios?*

294 To further validate our predictions, we examined how our models predicted *M. bovis* spread
295 across badger networks with empirical estimates using Shapley values (Shapley, 1951).
296 Shapley values are a game-theoretic approach to explore the relative contribution of each
297 predictor on individual networks (see *Methods*). While *M. bovis* in badgers often has a
298 prolonged latent period and individuals do not typically recover, generally *M. bovis* is a slow-
299 spreading infection, with an R_0 of between 1.1 and 1.3 (Delahay *et al.* 2013). Thus, we
300 interrogated our most similar model ($\beta = 0.05$, $\gamma = 0.04$, $R_0 = 1.25$). Our model predicted the
301 proportion of infected badgers in the network to be 0.45, which was much lower than the

302 average proportion infected across all networks included in our study (0.71, Fig. 5a). This
303 difference was largely driven by the badger network's low Fiedler value (0.096, much lower
304 than the mean of 7.31 across all networks) and, to a lesser degree, by the small spectral radius
305 (8.10 compared to a mean of 34.8 across all networks, Fig. 5a). This is comparable to
306 contemporaneous estimates of *M. bovis* prevalence in this population, e.g., 41% of badgers
307 tested in the network study tested positive (Weber *et al.* 2013).

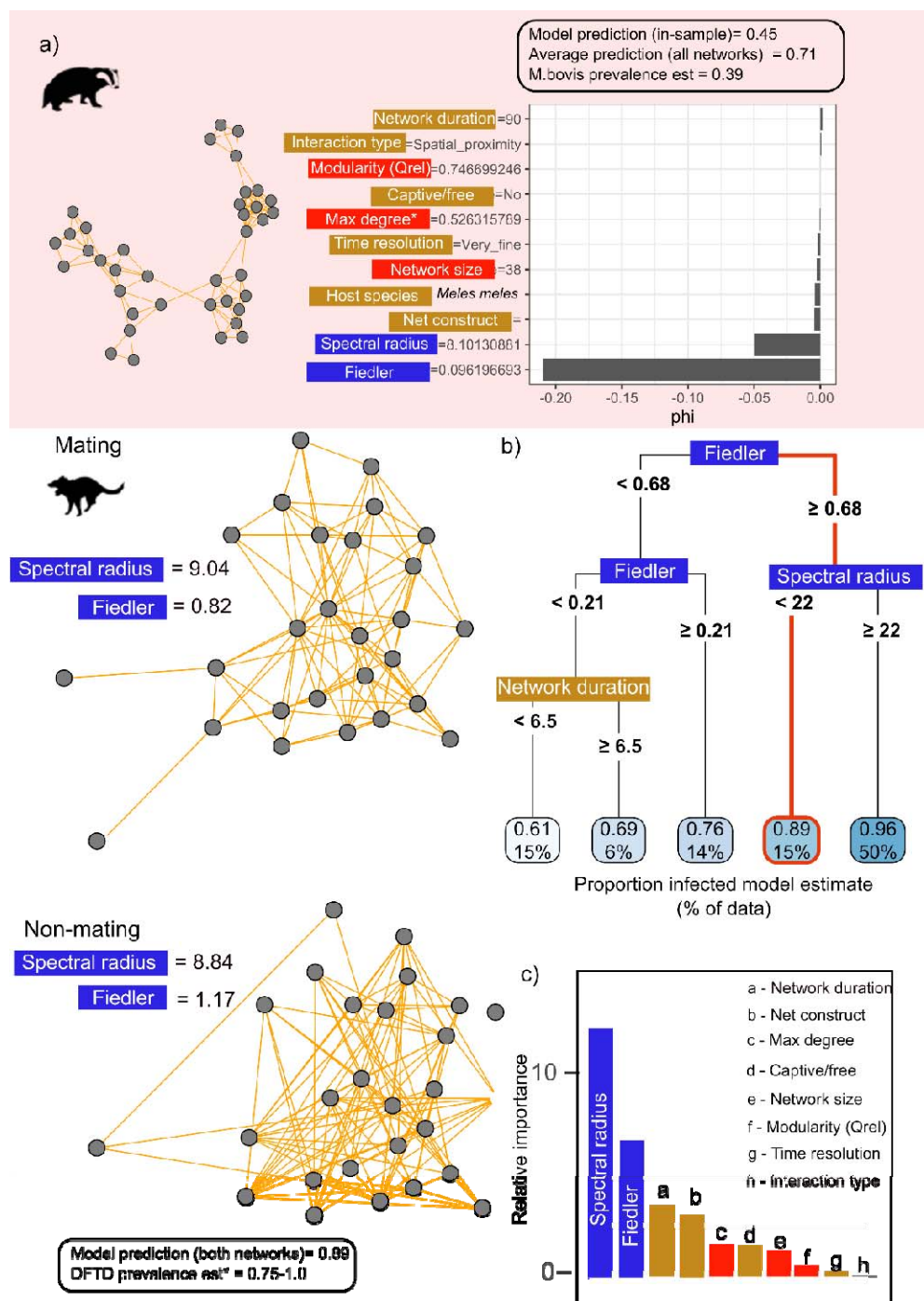
308

309 We further validated our approach using two Tasmanian devil contact networks (calibrated to
310 reflect potential DFTD transmission) not included in our training data (Fig. 5) and compared
311 to model estimate of spread to empirical observations in similar populations. Based on our
312 model that most closely mirrored devil facial tumour disease DFTD dynamics ($\beta = 0.2$, $\gamma =$
313 0.04, $R_0 = 5$, see Hamede *et al.* (2012)) we estimated the proportion infected to be 0.85-0.88
314 for mating and non-mating seasons respectively. Inputting the devil networks' Fiedler value
315 and spectral radius into the corresponding global surrogate model provides an estimate of
316 0.89 of individuals in the network infected (Fig. 5b). The spectral values were the most
317 important predictors in this model (Fig. 5c). Even though our simulations were not
318 formulated to model DFTD (e.g., devils rarely recover from DFTD), our machine-learning
319 estimates closely predicted the empirical findings for this disease. In comparable populations
320 across the island where the disease was monitored before the onset of the disease, maximum
321 prevalence estimates ranged from 0.7-1.0 in for sexually matured devils (≥ 2 y.o.) ~100
322 weeks after disease arrival (McCallum *et al.* 2009). Our predictions of proportion infected
323 were not particularly sensitive to transmissibility estimates as in our model. For example,
324 with a 50% reduction in the probability of transmission ($\beta = 0.1$) our estimate of proportion
325 infected was still similar to empirical estimates (0.83, Fig. S5a). Taken together, our findings

326 show how the spectral values of contact networks offer a valuable and informative

327 “shorthand” for how vulnerable different animal networks are to outbreaks.

328



329

330 **Fig. 5:** The spectral radius and the Fiedler underpinned our in-sample prediction of the
 331 proportion infected estimates in our a) badger and b/c) out-of-sample Tasmanian devil
 332 contact networks. a) Shapley values (ϕ) that quantify how each variable shaped simulated
 333 proportion infected ($\beta = 0.05$, $\gamma = 0.04$) in an empirical badger network. Negative Shapley
 334 values indicate that the variable reduced the proportion infection relative to other variables
 335 included in the model. See Fig S7 for other Shapley value analyses of other contrasting
 336 networks. b) Surrogate decision tree for the model that best approximated Tasmanian devil
 337 facial tumour disease (DFTD, $\beta = 0.2$, $\gamma = 0.04$). Red lines indicate the branches of the tree

338 corresponding to the spectral values from the left panels. The red outlined box is the
339 estimated proportion infected for both networks. c) Corresponding variable importance plot
340 showing the spectral radius and Fiedler value followed by data duration were the most
341 important predictors in the model. Colour of the labels indicates what type of predictor it is
342 (blue = spectral, red = non-spectral structural variables, gold = network metadata, see Tables
343 S2/S3). Panels on the left are the corresponding networks. Net construct = Network
344 construction method. *: for sexually mature individuals in comparable populations over
345 similar time scales to the simulations (McCallum *et al.* 2009).

346

347 **Discussion**

348

349 Here, we show that the spectral radius and Fiedler value of a network can be a remarkably
350 strong predictor for population vulnerability to diverse epidemics varying in key
351 epidemiological parameters. We demonstrate how a powerful machine learning and
352 simulation approach can effectively predict pathogen outbreak dynamics on a large collection
353 of empirical animal contact networks. We not only demonstrate the high predictive power of
354 a network's spectral properties but also show that our predictions can be a useful tool for
355 estimating spread in systems with complex disease dynamics. Our findings offer insights into
356 how nuances in social organisation translate into differences in pathogen spread across the
357 animal kingdom. Furthermore, our global surrogate models provide animal health
358 practitioners with an intuitive framework to gain rapid insights into the vulnerability of
359 populations to the spread of emerging infectious diseases.

360

361 Across real-world contact networks, we found that the networks' spectral properties (Fiedler
362 distance and spectral radius) were powerful proxies for pathogen spread. The strong
363 relationship between spectral radius and epidemic threshold has been demonstrated for
364 theoretical networks (Prakash *et al.* 2010) and has been used to assess vulnerability of cattle
365 movement networks to spread of bovine brucellosis (Darbon *et al.* 2018). We expand these
366 findings to show that the spectral radius is the most important predictor in our models of
367 epidemic behaviour across diverse animal social systems. While we examined only SIR

368 propagation through our networks, theoretical results suggest that our findings will extend to
369 other propagation mechanics such as SIS, (susceptible-infected-susceptible) and SEIR
370 (susceptible, exposed, infected, recovered) (Prakash *et al.* 2010). Given that both the badger
371 *M. bovis* and DFTD systems have more complex propagation mechanics compared to SIR,
372 our models could still predict disease dynamics of both disease systems reasonably well. We
373 that note that for DFTD, disease simulation models that assume homogeneous mixing of
374 hosts provide similar estimates of disease dynamics to network-based simulations (Hamede *et*
375 *al.* 2012). However, Hamede *et al.* (2012) found the outcome of simulated DFTD epidemics
376 sensitive to estimates of latent period and transmissibility parameters, whereas our network
377 structure approach provided realistic estimates of prevalence with minimal reliance on
378 parameter values.

379

380 For some networks and epidemiological parameters, spectral radius alone was not sufficient
381 to predict spread, and the Fiedler value and modularity still played an important role. The
382 Fiedler value and spectral radius of the networks were correlated, but below our $\rho = 0.7$
383 threshold (Fig. S2). One potential reason for this is that the Fiedler value seems to be less
384 sensitive to nodes with high connectivity compared to the spectral radius (Fig. 1); however,
385 the mathematical relationship between these two algebraic measures of connectivity is poorly
386 understood (Tang & Priebe 2016). Combined, our global surrogate models and accumulated
387 effects plots pointed to networks such as the devil networks with spectral radii $> \sim 8$ and
388 Fiedler values > 1 being more vulnerable to pathogen spread (the effect of the Fiedler value
389 on spread was much weaker overall). The spectral properties were dominant for the fast-
390 spreading pathogen models (e.g., example system), whereas network size and modularity
391 played a more important role in our models for more slowly spreading pathogens (e.g., Figs.
392 S5 & S6).

393

394 When modular structure played a role in disease spread in our study, we detected similar
395 patterns to those found by Sah *et al.* (2017). As in Sah *et al.* (2017), we found that epidemic
396 progression was only slowed in highly modular networks ($Q_{\text{rel}} > \sim 0.7$) when the probability
397 of transmission between nodes was low ($\beta > 0.025$). Such subdivided networks were rare in
398 our data and are commonly associated with high fragmentation (small groups or sub-groups)
399 and high subgroup cohesion (Sah *et al.* 2017). The reduced importance of modularity relative
400 to spectral radius is due to within-group connections being crucial for epidemic outcomes in
401 many contexts (Sah *et al.* 2017). Spectral values may have higher predictive performance, as
402 they summarize connectivity across the networks including between- and within-group
403 connections. Interpreting how modularity alone impacted epidemic outcomes was difficult on
404 these empirical networks, as all modularity measures were strongly correlated with mean
405 degree, diameter and transitivity (Fig. 2, Fig. S2). The extent of these correlations can vary
406 wildly based on other aspects of network structure and they all have interacting effects on
407 disease dynamics (Zhang & Zhang 2009; Ames *et al.* 2011). However, the spectral radius
408 captures epidemiologically important aspects of network structure on its own without having
409 to untangle whether different aspects of network structure are correlated.

410

411 More broadly, our study provides a framework for how interpretable machine learning can
412 predict spread across networks for a wide variety of epidemic parameters. While our RF
413 *MrIML* model had much higher predictive performance compared to the corresponding linear
414 models, further investigation of these models provided critical insight into how network
415 structure impacted pathogen spread. This framework could identify general trends of disease
416 vulnerability, specific thresholds for pathogens with certain characteristics, as well as the
417 drivers of spread for individual networks.

418

419 To help practitioners apply our model to different host-pathogen systems, we developed an
420 R-Shiny app (<https://spreadpredictr.shinyapps.io/spreadpredictr/>). Our web app allows users
421 to make predictions of spread for diverse transmission and recovery probabilities on a contact
422 network of interest without the need for simulation. Even when the underlying mechanism of
423 spread was mis-specified, as with our case studies, our model could provide reasonable
424 estimates of the proportion of the population infected that align closely with empirical data.

425 While currently limited to pathogens with SIR transmission dynamics, future versions of the
426 app will include, for example, SI and SEIR mechanics. We stress that for practitioners to
427 make accurate predictions for a particular pathogen, contact definitions and the duration of
428 data should be calibrated or multiple thresholds for what constitutes a transmission contact
429 assessed (see Craft 2015). For example, for the giraffe network we included edges that
430 represented individuals seen once together over a period of a year, and predictions of
431 pathogen spread on this network would likely be inflated for pathogens requiring more
432 sustained contact (VanderWaal *et al.* 2014). Nonetheless, this study shows the utility of
433 linking network simulation and interpretable machine learning approaches to tease apart the
434 drivers of spread across empirical wildlife networks

435

436 As this is a broad, comparative study of simulated pathogen spread on 603 empirical
437 networks across taxonomic groups, we made important simplifying assumptions. For
438 example, as there were large differences in how the empirical network edges were weighted
439 across taxa (e.g., some networks were weighted by contact duration and others by contact
440 frequency) our approach treated all contacts as equal in unweighted networks, as is done in
441 similar studies (Ames *et al.* 2011; Sah *et al.* 2017). We also simulated spread across static
442 networks, making the assumptions (i) that aggregated networks are representative or social

443 patterns at epidemiologically-relevant timescales and (ii) that network change happens more
444 slowly than pathogen spread. Including predictions of spread that account for the dynamic
445 nature of contact structure and pathogen-mediated changes in behaviour is an important
446 future extension of this work. However, applying dynamic network models such as temporal
447 exponential random graph models (Krivitsky & Handcock 2014) to estimate spread is
448 computationally demanding and challenging in a comparative setting due to idiosyncrasies in
449 the model-fitting process. While of high predictive value, our models did not capture all
450 aspects of uncertainty. For example, we assumed each network was fully described, with no
451 missing nodes or edges, which is almost always not the case for wildlife studies. How
452 sensitive spectral properties are to missing data is an open question. However, promisingly,
453 removing edges from ecological networks with high Fiedler values does not appear to
454 strongly impact the stability of the network (Kumar *et al.* 2019).

455

456 Another limitation of this study is that our models did not account for uncertainty in
457 predictions. Currently, more probabilistic models such as BART (Bayesian Additive
458 Regression Trees) (Carlson 2020) are not available in the *MrIML* framework, but future
459 extensions may allow for methods such as BART to be incorporated (Fountain-Jones *et al.*
460 2021). However, one advantage of our approach is that for the RF model (proportion
461 infected), host species (and the other categorical variables, see Table S3) could be added as a
462 categorical predictor rather than hot-encoded set of 43 predictors (one binary predictor for
463 each species (-1)). This simplified interpretations about how host species affect pathogen
464 spread differently, while accounting for nonindependence of intra-species networks (e.g.,
465 networks for host species A from different populations of that species or from different
466 timepoints) (Sah *et al.* 2019). A large proportion of the networks (~150) came from one taxon
467 (*C. fellah*); removing this one taxon did not qualitatively change our findings. While this

468 study demonstrates the power of repositories such as the ASNR, there are large biases in the
469 taxa covered that must be accounted for in model structure. Starting to fill in these taxonomic
470 gaps in a systematic way will increase the utility of comparative approaches such as ours and
471 make them generalizable across taxa and populations.

472

473 This paper provides a significant step towards a spectral understanding of pathogen spread in
474 animal networks. In particular, we show that the spectral radius of an animal network is a
475 powerful predictor of spread for diverse hosts and pathogens that can be a valuable shortcut
476 for stakeholders to understand the vulnerability of animal networks to disease. We also
477 demonstrate how multivariate interpretable machine learning models can provide novel
478 insights into spread across scales. Moreover, this study identified the key axes of network
479 structural variation across the animal kingdom that can inform future comparative network
480 research. As rapid advances in location-based tracking and bio-logging (Katzner & Arlettaz
481 2020) make network data more readily available to wildlife managers, approaches like this
482 one will be of increasing value.

483

484 **Methods**

485 *Networks*

486 We downloaded all animal contact networks from the ASNR on 12th January 2022 (Sah *et al.*
487 2019) and combined these with other comparable published animal contact networks
488 (Rushmore *et al.* 2013; Weber *et al.* 2013; VanderWaal *et al.* 2014). We binarized each
489 network, extracted the largest connected component, and excluded networks with fewer than
490 10 individuals. This left us with 603 networks from 43 species.

491

492 From each network we calculated a variety of network structure variables using the R
493 package *igraph* (Csárdi & Nepusz 2006) (see Table S2). As these networks were constructed
494 using a wide variety of techniques, we also extracted metadata from the ASNR or the
495 publication associated with the network (Table S3). These variables were also added to the
496 models. We used Principal Components Analysis (PCA) biplots to examine the drivers of
497 variation in network structure and visualise how networks clustered by taxonomic class. We
498 removed networks with missing metadata (8 networks) and screened for correlations between
499 variables. As many of the machine learning variables are less sensitive to collinearity
500 (Fountain-Jones *et al.* 2019) we used a pairwise correlation threshold of 0.7 and removed
501 variables from the pair with the highest overall correlation (Table S2).

502 *Simulations*

503

504 To simulate the spread of infection on each network we used our R package “EpicR”
505 (Epidemics by computers in R; available on GitHub at <https://github.com/mcharleston/epicr>).

506 The simulations use a standard discretisation of the SIR model, in which time proceeds in
507 “ticks,” for example representing days. Initially one individual was chosen at uniform random
508 to be infected (I) and all others were susceptible (S). At each time step, one of two changes of
509 state can happen to each individual (represented by a node), depending on its current state.
510 An ‘S’ individual will become infected (I) with a probability $(1 - (1 - \beta)^k)$, where k is the
511 number of currently infected neighbours it has, or otherwise stay as S; an ‘I’ individual will
512 recover (R) with probability γ or remain as I. Recovered (R) individuals stay as R.

513 In classical deterministic SIR models as a set of differential equations, β and γ are
514 instantaneous rates; here, they are probabilities per time step, so at a coarse level, they are
515 comparable.

516 On each network, we performed 1000 simulations using different combinations of
517 transmission ($\beta = 0.01, 0.025, 0.05, 0.1, 0.2$) and recovery probabilities ($\gamma = 0.04, 0.4$). We
518 chose these values to broadly reflect a range of scenarios from high to low transmissibility
519 and slow to fast recovery (Leung 2021) and ensure large outbreaks (>10% on individuals
520 infected, see Fig S8 for the analysis with a wider variety of recovery rates) (Sah *et al.* 2017).
521 For each simulation we recorded two complementary epidemic measures to capture disease
522 burden and speed of spread: a) the maximum prevalence reached, or the maximum proportion
523 of individuals infected in the network after 100 time steps and b) time to outbreak peak (i.e.,
524 which time step had the maximum number of infections). We chose 100 time steps to ensure
525 that the epidemic ended and there were no remaining infected nodes. One randomly chosen
526 individual was infected at the beginning of the simulation. The average maximum proportion
527 infected and time to outbreak across all simulations for each parameter combination were
528 used as the response variables in the machine learning models,

529

530 *Machine learning pipeline*

531

532 We used a recently developed multi-response interpretable machine learning approach (*Mr*
533 *IML*, Fountain-Jones *et al.* 2020) to predict outbreak characteristics using network structure
534 variables. Our *MrIML* approach had the advantage of allowing us to rapidly construct and
535 compare models across a variety of machine-learning algorithms for each of our response
536 variables as well as assess generalized predictive surfaces across epidemic parameters.

537

538 To test the robustness of our results, we compared the performance of four different
539 underlying supervised regression algorithms in our *MrIML* models. We compared linear
540 models (LMs), support vector machines (SVMs), random forests (RF) and gradient boosted

541 models (GBMs) as they operate in markedly different ways that can affect predictive
542 performance (Fountain-Jones *et al.* 2019; Machado *et al.* 2019). Categorical predictors such
543 as ‘species’ were hot-encoded for some models as needed (see Table S4). As both types of
544 responses in our models were continuous, we compared the performance of each algorithm
545 using the average R^2 and root mean squared error (RMSE) across all responses (hereafter, the
546 ‘global model’). As we included models that were not fit using sums of squares, our R^2
547 estimate depended on the squared correlation between the observed and predicted values
548 (Kvålseth 1985). As ants (Insecta: Formicinae) were over-represented, we compared model
549 performance and interpretation with and without these networks. To calculate each
550 performance metric, we used 10-fold cross validation to prevent overfitting each model. We
551 tuned hyperparameters for each model (where appropriate) using 100 different hyper-
552 parameter combinations (a 10×10 grid search) and selected the combination with the lowest
553 RMSE. The underlying algorithm with the highest predictive performance was interrogated
554 further.

555

556 We interpreted this final model using a variety of model-agnostic techniques within the
557 *MrIML* framework. We assessed overall and model-specific variable importance using a
558 variance-based method (Greenwell *et al.* 2018). We quantified how each variables alters
559 epidemic outcomes using accumulated local effects (ALEs) (Apley & Zhu 2016). In brief,
560 ALEs isolate the effect of each network characteristic on epidemic outcomes using a sliding
561 window approach calculating the average change in prediction across the values range (while
562 holding all other variables constant) (Molnar 2018). ALEs are less sensitive to correlations
563 and straightforward to interpret as points on the ALE curve are the difference from the mean
564 prediction (Apley & Zhu 2016; Molnar 2018; Fountain-Jones *et al.* 2021).

565

566 To further examine the predictive performance of our black-box models (SVM, RF and
567 GBM) we calculated a global surrogate decision tree (hereafter ‘global surrogate’) to
568 approximate the predictions of our more complex trained models. Global surrogates are
569 generated by training a simpler decision tree to the *predictions* (instead of observations) of
570 the more complex ‘black box’ models using the network structure data. How well the
571 surrogate model performed compared to the complex model is then estimated using R^2 . See
572 Molnar (2018) for details.

573

574 Lastly, we gained more insight into model behaviour and how network structure impacted
575 epidemic outcomes on individual networks, including by calculating Shapley values
576 (Štrumbelj & Kononenko 2014). Shapley values use a game theoretic approach to play off
577 variables in the model with each other based on their contribution to the prediction (Shapley
578 1953). For example, negative Shapley values indicate that the observed value ‘contributed to
579 the prediction’ by reducing the proportion infected or time to peak in an outbreak for a
580 particular network. See Molnar (2018) for a more detailed description and (Fountain-Jones *et*
581 *al.* 2019; Worsley-Tonks *et al.* 2020) for how they can be interpreted in epidemiological
582 settings.

583

584 We validated our results using networks with well-documented disease dynamics. The
585 European badger network was included in our training data, and we selected the propagation
586 model with a slow recovery rate ($\gamma = 0.04$) and intermediate transmissibility ($\beta = 0.05$) that
587 provided an equivalent/similar R_0 (1.1-1.3) to *M. bovis* in the studied badger population
588 (Delahay *et al.* 2013). It should be noted here that *M. bovis* infection has SEI(R)(D)

589 dynamics, being frequently latent in badgers for long periods with infection only resolving in
590 some individuals (the most infectious individuals with progressed disease have elevated
591 mortality (Corner *et al.* 2011)). We compared the proportion infected returned by our model
592 to various contemporaneous estimates of *M. bovis* prevalence (Delahay *et al.* 2013; Buzdugan
593 *et al.* 2017) in the long-term study that contact network data were collected in (McDonald *et*
594 *al.* 2018).

595 The Tasmanian devil networks were not included in the training data. To compare
596 predictions, we extracted the predict function from the model that was the most similar to
597 estimates of DFTD dynamics based on empirical data ($\beta = 0.2$, $\gamma = 0.04$, $R_0 = 5$) (McCallum
598 *et al.* 2009; Hamede *et al.* 2012). DFTD has SEI(D) dynamics in devil populations, however,
599 accurately estimating the latent period is impossible, as there is (as of May 2022) no
600 diagnostic tool to detect DFTD prior to visual detection of the tumours (Hamede *et al.* 2012).
601 As we wanted to make predictions on a species not included in our dataset, we reran the
602 models excluding the species predictor and the model performance, and results were very
603 similar. See <https://github.com/nfj1380/igraphEpi> for our complete analytical pipeline.

604 **Acknowledgements**

605 This project was supported by an Australian Research Council Discovery Project Grant
606 (DP190102020). We would also like to thank Prof. Menna Jones and Prof. Sue VandeWoude
607 for their support and comments on this manuscript.

608

609 **References**

610 Ames, G.M., George, D.B., Hampson, C.P., Kanarek, A.R., McBee, C.D., Lockwood, D.R.,
611 *et al.* (2011). Using network properties to predict disease dynamics on human contact
612 networks. *Proceedings of the Royal Society B: Biological Sciences*, 278, 3544–3550.

613 Apley, D.W. & Zhu, J. (2016). Visualizing the effects of predictor variables in black box
614 supervised learning models. *Journal of the Royal Statistical Society. Series B: Statistical
615 Methodology*, 82, 1059–1086.

616 Bansal, S., Grenfell, B.T. & Meyers, L.A. (2007). When individual behaviour matters:
617 homogeneous and network models in epidemiology. *J R Soc Interface*, 4, 879–891.

618 Bansal, S., Read, J., Pourbohloul, B. & Meyers, L.A. (2010). The dynamic nature of contact
619 networks in infectious disease epidemiology. *J Biol Dyn*, 4, 478–489.

620 Buzdugan, S.N., Vergne, T., Grosbois, V., Delahay, R.J. & Drewe, J.A. (2017). Inference of
621 the infection status of individuals using longitudinal testing data from cryptic populations:
622 Towards a probabilistic approach to diagnosis. *Sci Rep*, 7, 1111.

623 Carlson, C.J. (2020). *embarcadero*: Species distribution modelling with Bayesian additive
624 regression trees in R. *Methods in Ecology and Evolution*, 11, 850–858.

625 Corner, L.A.L., Murphy, D. & Gormley, E. (2011). *Mycobacterium bovis* Infection in the
626 Eurasian Badger (*Meles meles*): the disease, pathogenesis, epidemiology and control. *Journal
627 of Comparative Pathology*, 144, 1–24.

628 Craft, M.E. (2015). Infectious disease transmission and contact networks in wildlife and
629 livestock. *Philosophical transactions of the Royal Society of London. Series B, Biological
630 sciences*, 370, 20140107-.

631 Craft, M.E., Volz, E., Packer, C. & Meyers, L.A. (2011). Disease transmission in territorial
632 populations: the small-world network of Serengeti lions. *Journal of the Royal Society
633 Interface*, 8, 776–786.

634 Darbon, A., Valdano, E., Poletto, C., Giovannini, A., Savini, L., Candeloro, L., *et al.* (2018).
635 Network-based assessment of the vulnerability of Italian regions to bovine brucellosis.
636 *Preventive Veterinary Medicine*, 158, 25–34.

637 Delahay, R.J., Walker, N., Smith, G.S., Wilkinson, D., CLIFTON-HADLEY, R.S.,
638 Cheeseman, C.L., *et al.* (2013). Long-term temporal trends and estimated transmission rates
639 for *Mycobacterium bovis* infection in an undisturbed high-density badger (*Meles meles*)
640 population. *Epidemiology and Infection*, 141, 1445–1456.

641 Eames, K., Bansal, S., Frost, S. & Riley, S. (2015). Six challenges in measuring contact
642 networks for use in modelling. *Epidemics*, 10, 72–77.

643 Fountain-Jones, N., Kozakiewicz, C., Forester, B., Landguth, E., Carver, S., Charleston, M.,
644 *et al.* (2021). MrIML: Multi-response interpretable machine learning to map genomic
645 landscapes. *Molecular Ecology Resources*, 21, 2766–2781.

646 Fountain-Jones, N.M., Machado, G., Carver, S., Packer, C., Recamonde-Mendoza, M. &
647 Craft, M.E. (2019). How to make more from exposure data? An integrated machine learning
648 pipeline to predict pathogen exposure. *Journal of Animal Ecology*, 88.

649 Greenwell, B.M., Boehmke, B.C. & McCarthy, A.J. (2018). A simple and effective model-
650 based variable importance measure. *arXiv Preprint arXiv:1805.04755*.

651 Hamede, R., Bashford, J., Jones, M. & McCallum, H. (2012). Simulating devil facial tumour
652 disease outbreaks across empirically derived contact networks. *Journal of Applied Ecology*,
653 49, 447–456.

654 Hamede, R.K., Bashford, J., McCallum, H. & Jones, M. (2009). Contact networks in a wild
655 Tasmanian devil (*Sarcophilus harrisii*) population: using social network analysis to reveal
656 seasonal variability in social behaviour and its implications for transmission of devil facial
657 tumour disease. *Ecology Letters*, 12, 1147–1157.

658 Katzner, T.E. & Arlettaz, R. (2020). Evaluating contributions of recent tracking-based animal
659 movement ecology to conservation management. *Frontiers in Ecology and Evolution*, 7.

660 Krivitsky, P.N. & Handcock, M.S. (2014). A Separable Model for Dynamic Networks. *J R
661 Stat Soc Series B Stat Methodol*, 76, 29–46.

662 Kumar, D., Gupta, J. & Raha, S. (2019). Partitioning a reaction–diffusion ecological network
663 for dynamic stability. *Proc Math Phys Eng Sci*, 475, 20180524.

664 Kvålseth, T.O. (1985). Cautionary Note about R 2. *The American Statistician*, 39, 279–285.

665 Lentz, H.H.K., Selhorst, T. & Sokolov, I.M. (2012). Spread of infectious diseases in directed
666 and modular metapopulation networks. *Phys Rev E Stat Nonlin Soft Matter Phys*, 85, 066111.

667 Machado, G., Vilalta, C., Recamonde-Mendoza, M., Corzo, C., Torremorell, M., Perez, A., *et
668 al.* (2019). Identifying outbreaks of Porcine Epidemic Diarrhea virus through animal
669 movements and spatial neighborhoods. *Scientific Reports*, 9, 457.

670 McCabe, C.M. & Nunn, C.L. (2018). Effective network size predicted from simulations of
671 pathogen outbreaks through social networks provides a novel measure of structure-
672 standardized group size. *Frontiers in Veterinary Science*, 5.

673 McCallum, H., Jones, M., Hawkins, C., Hamede, R., Lachish, S., Sinn, D.L., *et al.* (2009).
674 Transmission dynamics of Tasmanian devil facial tumor disease may lead to disease-induced
675 extinction. *Ecology*, 90, 3379–3392.

676 McDonald, J.L., Robertson, A. & Silk, M.J. (2018). Wildlife disease ecology from the
677 individual to the population: Insights from a long-term study of a naturally infected European
678 badger population. *Journal of Animal Ecology*, 87, 101–112.

679 Meyers, L.A., Newman, M.E.J. & Pourbohloul, B. (2006). Predicting epidemics on directed
680 contact networks. *J Theor Biol*, 240, 400–418.

681 Meyers, L.A., Pourbohloul, B., Newman, M.E.J., Skowronski, D.M. & Brunham, R.C.
682 (2005). Network theory and SARS: predicting outbreak diversity. *J Theor Biol*, 232, 71–81.

683 Molnar, C. (2018). *Interpretable machine learning*. Retrieved from
684 <https://christophm.github.io/interpretable-ml-book/>.

685 Newman, M.E.J. (2002). The spread of epidemic disease on networks. *Physical Review E*, 66.

686 Newman, M.E.J. (2006). Community structure in social and biological networks.
687 *Proceedings of the National Academy of Sciences of the United States of America*, 99, 7821–
688 6.

689 Porter, M.A. (2020). Nonlinearity + Networks: A 2020 Vision. *Emerging Frontiers in*
690 *Nonlinear Science*, 32, 131–159.

691 Prakash, B.A., Chakrabarti, D., Faloutsos, M., Valler, N. & Faloutsos, C. (2010). Got the Flu
692 (or Mumps)? Check the Eigenvalue! *arXiv:1004.0060 [cond-mat, physics:physics, q-bio]*.

693 Rushmore, J., Caillaud, D., Matamba, L., Stumpf, R.M., Borgatti, S.P. & Altizer, S. (2013).
694 Social network analysis of wild chimpanzees provides insights for predicting infectious
695 disease risk. *Journal of Animal Ecology*, 82, 976–986.

696 Sah, P., Leu, S.T., Cross, P.C., Hudson, P.J. & Bansal, S. (2017). Unraveling the disease
697 consequences and mechanisms of modular structure in animal social networks. *PNAS*, 114,
698 4165–4170.

699 Sah, P., Mann, J. & Bansal, S. (2018). Disease implications of animal social network
700 structure: A synthesis across social systems. *Journal of Animal Ecology*, 87, 546–558.

701 Sah, P., Méndez, J.D. & Bansal, S. (2019). A multi-species repository of social networks. *Sci
702 Data*, 6, 44.

703 Sah, P., Otterstatter, M., Leu, S.T., Leviyang, S. & Bansal, S. (2021). Revealing mechanisms
704 of infectious disease spread through empirical contact networks. *PLOS Computational
705 Biology*, 17, e1009604.

706 Salathé, M. & Jones, J.H. (2010). Dynamics and Control of Diseases in Networks with
707 Community Structure. *PLOS Computational Biology*, 6, e1000736.

708 Shapley, L.S. (1953). Stochastic games. *Proceedings of the National Academy of Sciences of
709 the United States of America*, 39, 1095–1100.

710 Shu, P., Wang, W., Tang, M., Zhao, P. & Zhang, Y.-C. (2016). Recovery rate affects the
711 effective epidemic threshold with synchronous updating. *Chaos*, 26, 063108.

712 Silk, M.J., Croft, D.P., Delahay, R.J., Hodgson, D.J., Boots, M., Weber, N., *et al.* (2017).
713 Using Social Network Measures in Wildlife Disease Ecology, Epidemiology, and
714 Management. *Bioscience*, 67, 245–257.

715 Štrumbelj, E. & Kononenko, I. (2014). Explaining prediction models and individual
716 predictions with feature contributions. *Knowledge and Information Systems*, 41, 647–665.

717 Tang, M. & Priebe, C.E. (2016). Limit theorems for eigenvectors of the normalized Laplacian
718 for random graphs. *arXiv:1607.08601 [stat]*.

719 VanderWaal, K.L., Atwill, E.R., Isbell, L.A. & McCowan, B. (2014). Linking social and
720 pathogen transmission networks using microbial genetics in giraffe (*Giraffa camelopardalis*).
721 *The Journal of Animal Ecology*, 83, 406–14.

722 Weber, N., Carter, S.P., Dall, S.R.X., Delahay, R.J., McDonald, J.L., Bearhop, S., *et al.*
723 (2013). Badger social networks correlate with tuberculosis infection. *Current Biology*, 23,
724 R915–R916.

725 White, L.A., Forester, J.D. & Craft, M.E. (2017). Using contact networks to explore
726 mechanisms of parasite transmission in wildlife. *Biological Reviews*, 92, 389–409.

727 Worsley-Tonks, K.E.L., Escobar, L.E., Biek, R., Castaneda-Guzman, M., Craft, M.E.,
728 Streicker, D.G., *et al.* (2020). Using host traits to predict reservoir host species of rabies
729 virus. *PLOS Neglected Tropical Diseases*, 14, e0008940.

730 Zhang, Z. & Zhang, J. (2009). A big world inside small-world networks. *PLoS One*, 4, e5686.

731